JOURNAL OF THE KOREAN ASTRONOMICAL SOCIETY
38: 445 ~ 462, 2005

SPATIO-SPECTRAL MAXIMUM ENTROPY METHOD: II. SOLAR MICROWAVE IMAGING SPECTROSCOPY

SU-CHAN BONG[1], JEONGWOO LEE[2], DALE E. GARY[2], HONG SIK YUN[3], AND JONGCHUL CHAE[3]
[1]Korea Astronomy and Space Science Institute, 61-1 Hwaam-dong, Yuseong-gu, Daejeon, 305-348, Korea
E-mail: scbong@kasi.re.kr
[2]Physics Department, New Jersey Institute of Technology, Newark, NJ 07102, USA
E-mail: leej@njit.edu & dgary@njit.edu
[3]Astronomy Program, School of Earth and Environmental Science, Seoul National University, Seoul 151-747, Korea
E-mail: yun@astrosun.snu.ac.kr & chae@astro.snu.ac.kr
(Received October 11, 2005; Accepted November 16, 2005)

ABSTRACT

In a companion paper, we have presented so-called Spatio-Spectral Maximum Entropy Method (SSMEM) particularly designed for Fourier-Transform imaging over a wide spectral range. The SSMEM allows simultaneous acquisition of both spectral and spatial information and we consider it most suitable for imaging spectroscopy of solar microwave emission. In this paper, we run the SSMEM for a realistic model of solar microwave radiation and a model array resembling the Owens Valley Solar Array in order to identify and resolve possible issues in the application of the SSMEM to solar microwave imaging spectroscopy. We mainly concern ourselves with issues as to how the frequency dependent noise in the data and frequency-dependent variations of source size and background flux will affect the result of imaging spectroscopy under the SSMEM. We also test the capability of the SSMEM against other conventional techniques, CLEAN and MEM.

Key words : techniques: image processing – techniques: interferometric – techniques: spectroscopic – Sun: radio radiation

I. INTRODUCTION

This paper examines the performance of a technique for radio interferometric image reconstruction that we call the Spatio-Spectral Maximum Entropy Method (SSMEM). In a companion paper (Bong et al. 2005—Paper I), we extended the original ideas of Komm et al. (1997) from the 1D case to two spatial dimensions, and presented the 2D algorithm and its mathematical underpinnings. In this paper we wish to evaluate the technique for a model spectral brightness distribution, so that we can determine the usefulness of SSMEM in the case applicable to observations with the Owens Valley Solar Array (OVSA), i.e. the case of a sparse array observing solar continuum radio emission over 1–18 GHz. However, the method should have wide validity for similar cases where the observations pertain to slowly and smoothly varying spatial structure with frequency, for which measurements at sufficiently closely spaced frequencies ($\delta\nu/\nu \sim 0.1$) are available over a broad range ($\Delta\nu/\nu \sim 2$).

Solar microwave emission is mainly due to gyromagnetic radiation (Melrose 1980), which appears in the form of a broad spectrum. Interesting spectral features may occur in any part of the spectrum. Spectral diagnostics lead to the determination of physical parameters such as coronal magnetic field and electron temperature (Gary & Hurford 1994). Thus preserving the spectral morphology across a wide range of frequencies, perhaps over several octaves, is of major concern. SSMEM is expected to address this demand, since the brightness map at each frequency is constructed through communication with those at neighboring frequencies at the same spatial location (Paper I). The rationale of SSMEM is thus consistent with the scientific goal that we want to achieve through solar microwave observation. For instance we want to determine the spectral index within the data uncertainty, and SSMEM allows this determination consistent with the data.

In evaluating SSMEM as a tool for solar microwave imaging spectroscopy, we specifically consider possible difficulties arising in implementing solar imaging spectroscopy, and how the SSMEM can handle these problems. The solar-specific difficulties that we consider are as follows: (1) the radiation mechanism of solar microwave emission is closely associated with the magnetic field distribution in active regions. As a result the source size scales with magnetic field so that the morphology at a high frequency is determined by stronger field. In some cases it is also weighted by energetic particles. Since the magnetic field variation and energetic electron distribution are two intrinsic properties that we want to explore, an imaging technique that can handle the *uv* distribution variation with frequency, and that of intrinsic source variation is needed.

Corresponding Author: S.-C. Bong

(2) Solar phenomena are transient, and therefore snapshot mode rather than earth rotation synthesis is preferred. This will limit uv coverage unless the array has a large number of baselines. Some arrays, like OVSA, are designed to have many frequencies to measure the solar microwave spectrum, but consist of a relatively small number of baselines to be weak in imaging. At radio wavelengths, we have an opportunity to use the independent spatial information at adjacent frequencies to enhance the imaging through a technique called frequency synthesis (e.g. Conway et al. 1990; Sault & Wieringa 1994), but at the cost of frequency resolution. The SSMEM algorithm proposed in Paper I is an attempt to improve on frequency-synthesis by determining a source model that is the best fit globally to both the spatial and spectral information in the interferometer data. (3) In the case of solar radio observations the system temperature is dominated by the source. This is different from most other astronomical interferometry where thermal noise dominates the signal. It is necessary to understand the nature of noise in each case, which is a built-in feature in all MEM-type algorithms (Wernecke & D'Addario 1977, Gull & Daniell 1978, Skilling & Bryan 1984, Cornwell & Evans 1985, Narayan & Nityananda 1986, Cornwell et al. 1999). We will address the above-mentioned issues using the SSMEM presented in Paper I.

II. THE SSMEM

In this section, we outline the basic formultion of the SSMEM, the optimization techniques, and the convergence criteria used for the SSMEM.

(a) Basic Formulation

Astronomical MEMs define an object function J in terms of the spatial entropy, H, data constraint, χ^2, and flux constraint, F, and search for the solution map which maximizes J subject to the constraints. Since the SSMEM is meant to be an extension of the conventional MEM to include the frequency space as well as the xy plane, we introduce the frequency index k and treat each of the terms in conventional MEM object function as spectral components at the k-th frequency. The object function in the SSMEM is thus written in the following form:

$$J = \sum_k H_k - \sum_k \alpha_k \chi_k^2 - \sum_k \beta_k F_k + \gamma \sum_k S_k \quad (1)$$

The first three terms in the right hand side are usual MEM quantities that are defined as:

$$H_k = -\sum_j T_{jk} \ln\left(\frac{T_{jk}}{m_{jk}e}\right) \quad (2)$$

$$\chi_k^2 = \sum_i \frac{|V_{ik} - V'_{ik}|^2}{\sigma_{ik}^2} - n_{V_k} \quad (3)$$

$$F_k = \sum_j T_{jk} - F'_k, \quad (4)$$

where T_{jk} and m_{jk} are, respectively, the map temperature and default temperature at the j-th pixel and k-th frequency; V_{ik} and V'_{ik} are the calculated and observed visibilities at the i-th baseline and k-th frequency; n_{V_k} and σ_{ik} are the total number and standard deviation of V'_{ik}, respectively. A main difference of SSMEM from MEM lies in the last term, S_k, called the spectral entropy, which is introduced as a mechanism for exchanging information across frequencies (Komm et al. 1997). The spectral entropy is defined as

$$S_k = -\sum_j \tau_{jk} \ln\left(\frac{\tau_{jk}}{m_{jk}e}\right) \quad \text{with} \quad \tau_{jk} = m_{jk} + |T_{jk} - \langle T_{jk}\rangle| \quad (5)$$

where $\langle T_{jk}\rangle$ is the logarithmically interpolated temperature from adjacent frequencies (See, for more details, Paper I). Were there no other constraint, S_k will be maximized when $T_{jk} = \langle T_{jk}\rangle$, and the spectrum at a given spatial position follows a power law function of frequency as we intended. A multiplicative factor, γ plays a role of leveraging the relative importance of the spectral entropy to the spatial entropy. $\gamma = 0$ corresponds to conventional MEM. In Paper I we have shown that setting this factor to unity leads to adequate results.

(b) Optimization Techniques

Optimization of the entropy consists of the maximization of the object function and adjustment of the Lagrangian multipliers so that the constraints are satisfied. We express these two steps in terms of two sets of equations:

$$\nabla_T J = 0 \quad \text{and} \quad f(z) = 0 \quad (6)$$

The new quantity $f(z)$ is a multi-variate vector function defined as:

$$f(z) = \{\chi_k^2, F_k\} \quad \text{and} \quad z = \{\alpha_k, \beta_k\}, \quad k = 1, \cdots, n_\nu \quad (7)$$

In general, we can think of two techniques for solving these equations. In a conservative approach, we may solve the first equation $\nabla J = 0$ to get the map T_{jk} under fixed Lagrangian multipliers and then solve the second equation $f(z) = 0$ with the temperatures obtained in the previous step, which repeat until both sets of equations are satisfied altogether. Second method is to use a modified Newton-Raphson (NR) method, which allows $\{\alpha_k, \beta_k\}$ and $\{T_{jk}\}$ to be advanced simultaneously (Cornwell & Evans 1985; Sault 1990). We will implement both approaches in this section and decide later which one is more suitable for our SSMEM based on the result in the next section.

i) Sault's Algorithm

In Sault's (1990) formulation, the Lagrangian multipliers, as well as the temperatures, are regraded as variables of the object function (hence in the present case, $J = J(\{T_{jk}\}, \{\alpha_k\}, \{\beta_k\})$ with $j = 1, \cdots, n_T$ and $k = 1, \cdots, n_\nu$). This formulation then reveals that the above-defined constraint function $f(z) = 0$ corresponds to $\{\partial J/\partial\alpha_k, \partial J/\partial\beta_k\} = 0$. Therefore the two sets of equations in equation (6) can be unified into a set of equations:

$$\nabla_\xi J = 0 \tag{8}$$

where $\xi = \{T_{jk}, \alpha_k, \beta_k\}$. Since both sets of the equations now look alike, this formulation naturally encourages simultaneous adjustment of the temperature and Lagrangian parameters in one step. Cornwell/Evans (1985) and Sault (1990) suggest to solve the equation by the NR method:

$$\delta\xi = -(\nabla_\xi \nabla_\xi J)^{-1} \cdot \nabla_\xi J \tag{9}$$

However, the Hessian matrix $\nabla_\xi \nabla_\xi J$ is huge in size, and a modification from the standard NR has been suggested. That is to ignore the off-diagonal elements of the matrix $\nabla_T \nabla_T J$ as a justifiable approximation (Cornwell & Evans 1985).

To use this approach for our SSMEM, we simply extend ξ (and accordingly the Hessian matrix) to include the frequency space. The resulting Hessian matrix $\nabla_\xi \nabla_\xi J$ when expressed in terms of $\nabla_T \nabla_T J$, $\nabla_T \chi_k^2$ and $\nabla_T F_k$, takes the same form as that of Sault (1990), with a trivial difference in the additional frequency index k and is thus not reproduced here. An important difference lies, however, in the fact that the present $\nabla_T \nabla_T J$ contains additional off-diagonal elements associated with the spectral entropy term, i.e., $\nabla_T \nabla_T S$. We will use only the diagonal elements of $\nabla_T \nabla_T S$ as well as other diagonal elements as a test of the modified NR method, without actually knowing at this stage how this approximation will affect the convergence in the present SSMEM. We shall examine the results of this test and compare with an alternative method in §3.2.1.

We however make a simple remedy in an attempt to make our spectral entropy calculation more consistent with the Cornwell/Evan's approximation. The off-diagonal components of $\nabla_T \nabla_T S$ arise because spectral entropy at one spatial location and a frequency (say S_{jk}) depends not only on the temperature at that location (T_{jk}) but on the temperatures at neighboring frequencies ($\widetilde{T}_{jk}^{\pm}$), and each of the latter two temperatures are again related to four nearby temperatures via the interpolation factor $R_{jkj'k'}$ (see eq. [4]–[7] and Figure 1 of Paper I). When these (total eight) neighboring temperatures are adjusted, they will contribute to the final adjustment of $\delta\xi$. A net result of ignoring their contribution is then an overestimation of $\delta\xi$. This can be prevented by boosting up the diagonal elements of $\nabla_T \nabla_T S_{jk}$ to compensate the missing contribution from the off-diagonal elements. For this purpose we rescale the diagonal component of $\nabla_T \nabla_T S_{jk}$ in the above calculation using the interpolation factors:

$$\frac{\partial^2 S_{jk}}{\partial T_{j'k'}^2} \rightarrow g_{jkj'k'} \frac{\partial^2 S_{jk}}{\partial T_{j'k'}^2} \tag{10}$$

with

$$g_{jkj'k'} = \frac{2}{\delta_{jj'}\delta_{kk'} + a_k^+ R_{jkj'k'}^+ + a_k^- R_{jkj'k'}^-} \tag{11}$$

The factor 2 appears in the numerator, because S_{jk} is determined by T_{jk} and $\langle T_{jk} \rangle$, and the latter is determined using temperatures at two neighboring frequencies along with the interpolation factors, $a_k^{\pm}$. The other interpolation factor $R_{jkj'k'}^{\pm}$ appears here to make all the four nearby temperatures adjusted by equal amount. This boosting factor is equal to or greater than unity so as to prevent overestimation of $\delta\xi$ (see eq. [9]).

ii) A Conservative Algorithm

We also consider an alternative optimization technique that makes use of only the first derivative of the object function. A motivation is, of course, the fact that the above approximation of the Hessian matrix of J (i.e., excluding off-diagonal elements of $\nabla_T \nabla_T S$) can be avoided and it can thus serve as a cross-check. In this effort, we take a conservative approach, in which the two sets of equations in equation (6) are solved in separate stages, namely, we first solve $\nabla_T J = 0$ with fixed z and use the solution $\{T_{jk}\}$ in solving $f(z) = 0$ in one cycle of optimization. The updated z are then fed into the next cycle of maximization, which repeats until we get complete solutions to equation (6).

The reason why we intend to solve $\nabla_T J = 0$ separately from $f(z) = 0$ is that the former simply represents a problem of finding the maxima of J in a multivariate space T_{jk} and can thus be solved using an alternative maximum searching algorithm such as Conjugate Gradient (CG) Method (Press et al. 1992, p. 420). On the other hand, the latter equation $f(z) = 0$ represents neither maximization nor minimization conditions, but rather a problem of finding roots of the equation. Therefore the solution to this equation can be found more suitably by NR Method rather than by a maximum search algorithm. The NR equation, in this case, takes the form:

$$\delta z = -\mathbf{C}^{-1} \cdot f \tag{12}$$

where $\mathbf{C}$ is a Jacobian matrix defined by $C_{pq} = \partial f_p / \partial z_q$ and p and q are indexes running from 1 to $2n_\nu$. Although at the beginning this Jacobian matrix has to be created fully by taking all derivatives of f with respect to the set of Lagrangian multipliers z, later on we can reuse the initial matrix obtained, to find the next one by a faster method, Broyden's method (Press et al. 1992, p. 389).

The CG method utilizes only the first derivative of the object function. Cornwell & Evans (1985) pointed out that any algorithms employing only the first derivative may lead to a problematic steep gradient near small temperature due to the functional form of the entropy. To address this problem, we introduce a change of variable from T to some other variable ζ which will guarantee the gradient of J defined with respect to ζ behaves well at low T. We consider ζ defined by

$$\zeta_{jk} = \frac{T_{jk}}{m_{jk}} - \frac{m_{jk}}{T_{jk}} \tag{13}$$

where m_{jk} is the default map at pixel j and frequency k. This quantity ζ behaves similar to T for $T \geq m$ ($\zeta \geq 0$) and this change of variable is not much different from the original formulation. ζ is mainly introduced for the range of $0 < T < m$ ($-\infty < \zeta < 0$) where $\zeta \sim -T^{-1}$ and has an effect of slowing down the rapid divergence of the gradient, avoiding the overshooting problem in low T. We thus replace the gradient in T space with that in ζ space, i.e., $\partial/\partial\zeta_{jk} = (dT_{jk}/d\zeta_{jk})\partial/\partial T_{jk}$. We argue that since $(dT/d\zeta)$ is positive and bounded, $\nabla_\zeta J = 0$ is equivalent to $\nabla_T J = 0$.

To close this section, we summarize the advantages of each method. The Sault's method is based on a modified NR technique and leads to coherent treatment of both temperatures and Lagrangian parameters and can be considered an efficient method. The second method based on CG involves no approximation, and also skips the calculation of the second gradient of the object function. It however performs maximization of J and adjustment of Lagrangian parameters separately, which can be viewed as inefficient. It is our goal in §3.2.1 to compare capabilities of the NR and CG methods based on actual simulation result.

(c) Convergence Criteria

It is often arbitrary to define the criteria for $\nabla J = 0$ and $f(z) = 0$ and the criteria must be tied to the optimization technique used. In the present formulation, we consider that ∇J approaches to zero closely enough if its magnitude becomes smaller than a fraction of the magnitude of the vector sum of its constituent terms. For the constraints, we may consider $f = 0$ is satisfied if its absolute values $\{|\chi^2_k|, |F_k|\}$ are small compared with $\{n_{Vk}, F'_k\}$ or comparable to their uncertainties. We wish to have the convergence criteria essentially the same for both methods, so that the resulting solutions are consistent with each other. However there are inevitably a few minor differences, as described below. From this point on, we will simply call the two optimization techniques in §2.2.1 and §2.2.2 by NR and CG methods, respectively.

i) Criteria under the NR Method

To set the criterion for map convergence, the magnitude of $\nabla_T J$ needs to be defined. Since this is a vector quantity and the criterion should also be met at each frequency, we define the magnitude of the vector in the row corresponding to the k-th frequency as:

$$|\nabla_T J|_k = \sqrt{\sum_{j=1}^{n_T} \left(\frac{\partial J}{\partial T_{jk}}\right)^2}$$

We want this quantity to be smaller than a small fraction of that of the constituent terms,

$$|\nabla_T J|_k \leq \epsilon \sqrt{\begin{array}{l} |\nabla_T H_k|^2 + \alpha_k^2 |\nabla_T \chi_k^2|^2 \\ \quad + \beta_k^2 |\nabla_T F_k|^2 + \gamma^2 |\nabla_T S|_k^2 \end{array}} \tag{14}$$

where we set ϵ to a small value, $\epsilon = 0.03$.

For the criteria of the constraints, we may consider f as having converged if its absolute values $\{|\chi^2_k|, |F_k|\}$ are small compared with $\{n_{Vk}, F'_k\}$ or comparable to their uncertainties. We thus set the criteria for the constraints as

$$|\chi^2_k| \leq \max(\epsilon n_{Vk}, \delta\chi^2_k) \tag{15a}$$
$$|F_k| \leq \max(\epsilon F'_k, \delta F_k) \tag{15b}$$

for every frequency k. Now the uncertainties in the constraints χ^2_k and F_k would simply be

$$\delta\chi^2_k = \sqrt{2n_{Vk}} \tag{16a}$$
$$\delta F_k = \delta F'_k \tag{16b}$$

$\sqrt{2n_{Vk}}$ is the standard deviation of the chi-square distribution, and $\delta F'_k$ is the uncertainty of F'_k given as an input parameter.

ii) Criteria under the CG Method

To have the criteria for CG method consistent with those of NR method, we have to make a few minor modifications. First of all, under the CG method, the differentiation is made with respect to ζ instead of T, and the above definition of the magnitude of $\nabla_T J$ is replaced with $\nabla_\zeta J$. We also introduce spectral weights w_k for each spectral object function, J_k, in the CG method so that J is modified to $J = \sum_{k'} w_{k'} J_{k'}$. This is to prevent a case in which the gradient of J at a particular frequency dominates over others at the remaining frequencies, and thus dominates the whole process of maximization. For this purpose we normalize the χ^2 term of each frequency by setting $w_k = (\alpha_k n_{Vk})^{-1}$. Thus a modified form of equation (14),

$$|\nabla_\zeta J|_k \leq \epsilon \sqrt{\begin{array}{l} w_k^2 |\nabla_\zeta H_k|^2 + w_k^2 \alpha_k^2 |\nabla_\zeta \chi_k^2|^2 \\ \quad + w_k^2 \beta_k^2 |\nabla_\zeta F_k|^2 + \gamma^2 |\nabla_\zeta S|_k^2 \end{array}} \tag{17}$$

is used for the maximization criterion under the CG method, where S is also modified to $S = \sum_{k'} w_{k'} S_{k'}$.

Under the CG method, $\{\chi^2_k\}$ and $\{F_k\}$ are known after the maximization. The maximization is achieved

only approximately within its convergence criteria, and the achieved $\{\chi_k^2\}$ and $\{F_k\}$ may be different from those at the true maximum point. The differences would be related to the final change $\delta\zeta$, if the true maximum point is located within the range of $[\sum_j(\delta\zeta_{jk})^2]^{1/2}$ at each frequency. We are thus led to modify the ranges of uncertainty, $\delta\chi_k^2$ and δF_k as

$$\delta\chi_k^2 = \max\left(|\nabla_\zeta\chi_k^2|\sqrt{\sum_j(\delta\zeta_{jk})^2}, \sqrt{2n_{V_k}}\right) \quad (18a)$$

$$\delta F_k = \max\left(|\nabla_\zeta F_k|\sqrt{\sum_j(\delta\zeta_{jk})^2}, \delta F_k'\right) \quad (18b)$$

Since we require these criteria to be met at all frequencies, sometimes the iteration may have to continue although the criteria are satisfied at many frequencies. Although this may slow down the overall process, we give weight to the more accurate solution rather than the faster process in CG method.

III. APPLICATION

(a) Models

Since the goal of our investigation is how SSMEM can help with solar microwave imaging spectroscopy, we carefully design a model that we believe has characteristics of solar microwave radiation as described in §1. We mainly focus on three model parameters: the source size, signal-to-noise ratio of the data, and background flux, which are set to vary with frequency in a specified way. The latter two elements may be insignificant factors in other imaging algorithms, but are significant here because of their major role in the MEM algorithm. An important aspect of this investigation is to determine how the frequency dependence of these factors may affect the science drawn from the imaging spectroscopy.

i) Array and Source

For the model array, we take the OVSA antenna locations (Gary & Hurford 1999). The array configuration and the corresponding uv distribution are shown in Figure 1(a) and (b) respectively. The system consists of 7 antennas, which gives 21 baselines or equivalently 21 uv points at a time. The number of uv points is rather small and the uv coverage is highly asymmetric, as shown in the figure. It is therefore of interest to determine to what extent the SSMEM helps in overcoming this poor uv sampling.

We create the radiation source and its frequency variation to mimic real sources on the Sun. Such sources are typically dominated by either single/double Gaussians or single curved ellipse, because the radiating electrons are trapped in magnetic loops connecting two footpoints or bipolar sunspots (see, e.g., Aschwanden et al., 2002). Active region sources generally maintain coronal temperature at low frequency and decrease at high frequency. The source size decreases with frequency because the higher frequency emission comes from stronger magnetic field (see, for instance, Dulk 1985). We thus use a combination of two Gaussians which are centered at (x_c, y_c) with peak temperature T_p and width w. The width decreases with frequency according to a power law

$$w = w_5\left(\frac{\nu}{5\text{ GHz}}\right)^{-C} \quad (19)$$

where w_5 is the width of the source at 5 GHz. The separation between the centers of the two Gaussians is fixed in our model. Schmahl & Hurford (2002) have shown that typical core size of hard X ray sources is $\sim 10''$. We choose compatible sizes and list them in Table 1. As a result, this model can simulate a single large source at low frequencies and a pair of double smaller sources at higher frequencies, which, we intend to simulate the large coronal loop source connecting bipolar sunspot sources. Whether the source size varies more or less rapidly with frequency compared with the beam is an important factor.

We denote the true, noiseless model temperatures as t_{jk} with j denoting map pixel and k frequency as before, which is then Fast-Fourier-Transformed into the uv plane to obtain true visibilities:

$$\widehat{V}_{jk}^{\rm t} = \sum_{j'} t_{j'k}e^{2\pi i\mathbf{u}_{jk}\cdot\mathbf{x}_{j'k}} \quad (20)$$

in units of solar flux units (sfu)*. The true observed visibility, $V_{ik}^{\rm t}$, at the preset (u, v) point of each baseline i (Fig. 1(b)) is then interpolated from the above visibility in the uv grid, $\widehat{V}_{jk}^{\rm t}$, and is used for computation of χ^2.

ii) Noise

We create the observed visibilities V_{ik}' by adding noise at each baseline i and frequency k, according to the rule:

$$V_{ik}' = V_{ik}^{\rm t} + N\sigma_{ik} \quad (21)$$

*1 sfu = 10^4 Jy = 10^{-22} W m^{-2} Hz^{-1}

TABLE 1.
GAUSSIAN SOURCE PARAMETERS AT 5 GHZ

Source	T_p (MK)	x_c ($''$)	y_c ($''$)	w_5 ($''$)
1	2.0	10	5	10
2	1.5	−15	0	7

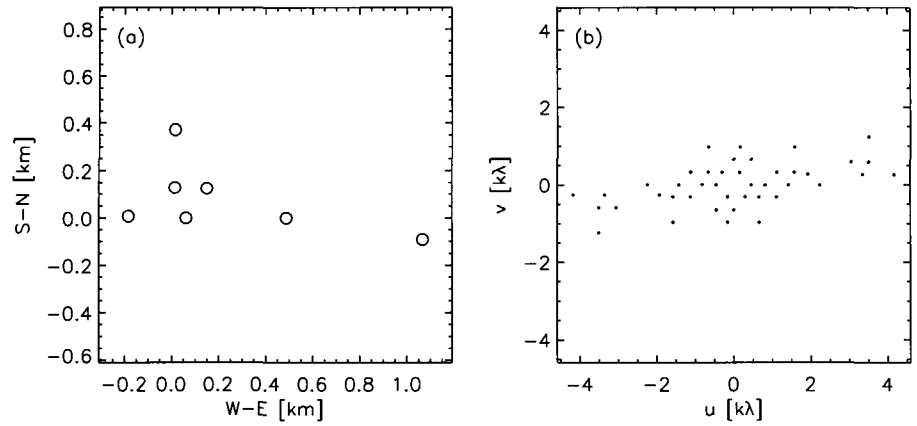

Fig. 1.— Model uv distribution as used in the tests. (a) Antenna configuration of OVSA. Geographic north is up and east is to the right. Each circle represents an antenna position. (b) Snapshot uv coverage at 1 GHz resulting from the OVSA antenna configuration. Here, u points in the west and v points north.

where N is a random complex variable with Gaussian distribution of unit variance, and σ_{ik} is the standard deviation of the noise. The noise in the visibility arises from the antenna-based noise, which depends on many factors. Although this is much of a hardware design issue, we make a simple investigation on a plausible form of the noise-contaminated visibility in Appendix A. We focus on how the noise in the visibility should depend on that of antennas in the case of a solar observation†. The idea is as follows: in conventional astronomical interferometry, the antenna noise dominates the signal, and the correlated signal from two antennas is also dominated by the product of noise from each antenna. Therefore the correlated noise could be handled independent of the signal strength. This is typically not true for solar interferometry, where the system temperature is dominated by the high flux density of the Sun, and as a result, the visibility will include the product of noise from one antenna and signal from another antenna. As described in Appendix A, if the antenna noise is proportional to the source flux density, as in the solar case, then the standard deviation is proportional to the visibility amplitude $\sigma \propto |V|$. We assume this dependence for the noise in the models presented here. In addition there can (in general) be white noise introduced to the correlated signal. Under this consideration, we use a standard deviation in the following form:

$$\sigma_{ik} = A|V^{\rm t}_{ik}| + B \qquad (22)$$

The noise is thus parameterized by A and B in units of sfu, which represent the amplitude dependent part and the white noise, respectively. We will set A and B to be independent of frequency merely for convenience. Since the solar intensity generally increases at low frequencies and decreases at high frequencies, as does the visibility amplitude $|V|$, equation (13) implies that we impose a relatively larger amount of noise to the visibility at higher frequencies, which might have a systematic effect on the imaging. We regard this as another important issue that should be addressed by solar microwave imaging spectroscopy.

iii) Background Flux

The background temperature is a factor in the MEM algorithm (as opposed to the CLEAN algorithm where the background flux is zero) because the temperature should be positive everywhere by definition. The choice of background flux in MEM is important since we adopt the flux as a constraint following Cornwell & Evans (1985). For instance, the background flux, if set too low, may lead to a situation where a solution satisfying the a priori of positivity no longer exists. This problem vanishes as we increase the background temperature to some level. A problem is whether or how the resulting map depends on the background temperature level.

In the present model we consider the background flux only as an internal parameter. For solar flare data processing, it is conventional to subtract the background to determine the flare generated flux only. The background flux we add here is then the flux of a flat background temperature $T_\nu^{\rm bg}$ which is introduced for mapping purposes only. We therefore consider it worthwhile to investigate this effect by using SSMEM models with different choice of background temperature. To minimize any frequency dependent effect associated with the background, we use a parameter D as the contrast against the maximum brightness temperature in

†The idea has been inspired by D. Emerson's presentation during Frequency-Agile Solar Radiotelescope (FASR) science definition workshop held in Green Bank, WV, USA, 23–25 May, 2002.

the map, independent of frequency:

$$T_\nu^{\rm bg} = D \max(T_\nu^{\rm src}) \quad (23)$$

Under the considerations given above, we create seven different models as summarized in Table 2. Model 1 has the most probable data noise prescribed with $A = 0.03$ and $B = 0.02$ sfu, and an ideal source variation with frequency that goes with the beam size, with $C = 1$. Taking model 1 as our reference model, we take A and B ten times greater in models 2 and 3, respectively. In models 4 and 5 we use different source size variations with frequency, i.e., $C = 1.5$ and 0.5. $D = 0.3\%$ is used as a typical case of arbitrary background flux level, and is varied in models 6 and 7 to 0.03% and 3.0%, respectively.

(b) Results

We run SSMEM on the seven models listed in Table 2 to investigate the effect of various model parameters on the result of spectral map reconstruction. In addition we also compare the results with other methods of image reconstruction: CLEAN maps obtained using the Högbom (1974) algorithm and conventional MEM maps obtained in the present SSMEM simply by excluding the spectral entropy term from equation (1).

i) Efficiency of the Optimization Algorithms

We first check whether the quality of final maps depends on the optimization technique using model 1. The results are shown in Figure 2. The top panels (a)–(c) shows the 2D maps reconstructed using the NR (CG) optimization techniques as contours of solid (dashed) lines on top of the true source shown as greyscale image. The reconstructed maps show somewhat elongated features at all frequencies compared with the true source (especially at 5.0 GHz), which is due to the small number of baselines along north-south direction. Otherwise the reconstructed maps are close to the true models at all frequencies with little difference between the two optimization techniques. Panels (d)–(f) show the 1D scans of the maps along the $y = 5''$, which reveal slight differences between the two methods, especially near the peak. The CG method yields a higher but a little bit underestimated peak temperature, whereas the NR yields a lower profile around the peak temperature at 1.8 GHz. At other frequencies the 1D maps are more coincident to each other. Panel (g) shows the 1D scan along $x = 10''$ where the uv points are relatively deficient. Here it reveals little differences between the two methods. The last two panels (h) and (i) show local spectra measured at the position of the two local maxima. The difference between two results is again very subtle, compared with the difference from the true spectra. It therefore appears that the NR approach is practically good enough compared to the CG approach, in spite of the approximations made in the calculation of $\nabla\nabla J$. Figure 2 also demonstrates that we were successful in making the convergence criteria applied to both methods equivalent.

TABLE 2.
TRUE MODEL PARAMETERS

Model	A	B (sfu)	C	D (%)
1	0.03	0.02	1.0	0.3
2	0.3	0.02	1.0	0.3
3	0.03	0.2	1.0	0.3
4	0.03	0.02	1.5	0.3
5	0.03	0.02	0.5	0.3
6	0.03	0.02	1.0	0.03
7	0.03	0.02	1.0	3.0

As both optimization techniques yield similar final map quality, we examine the efficiency of each technique as a main factor. We make this test for six different cases that differ in terms of γ and uv coverage, and list the results in Table 3. The tests are made in terms of the average time spent in computing the gradient in the units of seconds, the number of calls to the gradient computation routine, and the total time required to finish the job, respectively, as listed in the fourth to sixth columns. The corresponding results are given as a pair of numbers divided by slash per item. The numbers before and after each slash are the results obtained with the NR and CG methods, respectively.

As the fourth column of Table 3 shows, the average time spent in calculation of the gradient per optimization cycle is shorter when the CG method is used in the presence of the spectral entropy term (i.e., $\gamma > 0$). This computation takes longer under the NR method because it requires additional calculation of the second derivatives. However, as the fifth column shows, the number of calls to the gradient calculation is always higher under the CG method, because more frequent adjustment of the search direction has to be made. As a result, the NR outperforms the CG method in total computing time (the last column). The same trend is seen even though spectral entropy term is weighted up. Namely, when we increase γ from 1 to 3, the total computing time under the NR method does not change significantly. This implies that our adjustment of the gradient of spectral entropy (eq. [10] and [11]) works to properly compensate the ignored off-diagonal terms in NR. On the other hand, the total computing time under the CG method is sensitive to γ. This is mostly due to increased burden in calculation of the Jacobian matrix $\mathbf{C}$ (eq. [12]) with large γ. The similar trend continues when we adopt a much better uv coverage. The only difference was that the uv coverage synthesized over 4 hours required almost a factor of 10 more time than the snapshot uv coverage. In addition, we note that the NR method becomes much more efficient than the CG method when the map size is larger. For

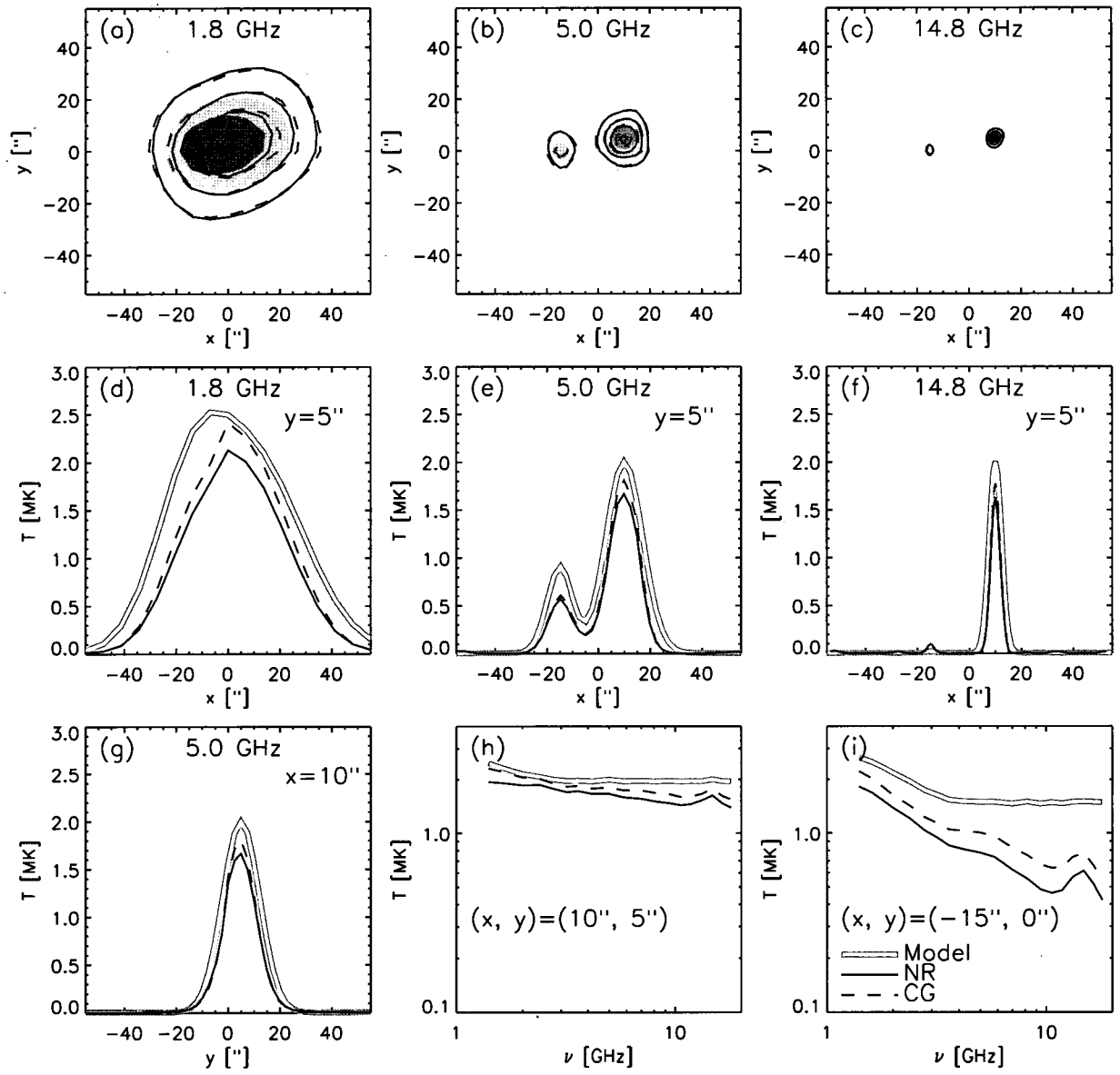

Fig. 2.— Test run of SSMEM using the NR and CG optimization techniques with $\gamma = 1$. Top panels show maps at (a) 1.8 GHz, (b) 5.0 GHz, and (c) 14.8 GHz, respectively. The true source is shown as grey image and the contours are the reconstructed images using NR (solid line) and CG (dashed line) methods. The contour levels increase by 20% of the maximum of the true source. Middle panels: (d)–(f) show 1-D scan of the maps shown in the top panels along $y = 5''$. Bottom panels: (g) is 1-D scan of the maps at $x = 10''$. (h) and (i) are the local spectra measured at the position of two local maxima: $(x, y) = (10'', 5'')$ and $(-15'', 0'')$, respectively.

TABLE 3.
PROGRAM PARAMETERS

Case	γ	uv Coverage	Grad. Avg. (s)	Grad. Call	Total (s)
1	3	Snapshot	2.8/2.4	940/ 2400	3400/ 6200
2	1	Snapshot	2.8/2.3	770/ 1500	2800/ 4000
3	0	Snapshot	1.1/1.3	510/ 1400	990/ 2200
4	3	4hr-Synthesis	2.8/2.4	6100/29000	22000/77000
5	1	4hr-Synthesis	2.8/2.3	6600/15000	24000/38000
6	0	4hr-Synthesis	1.1/1.3	7400/10000	14000/16000

Test is made using IDL 6.0 on a Windows PC having 500 MHz Pentium III CPU and 256 MB RAM.

instance, when we increased the map size from 128×128 to 256×256 pixels, we found that the running time under NR increases just in proportion to the pixel number (i.e., 4 times longer than the cases presented in Table 3), because the gradient is treated on pixel by pixel bases. However, the CG method needs a much longer search time, as the variable space where the solution is searched through becomes wider. To summarize, NR outperforms CG irrespective of the spectral entropy weight and the uv coverage.

ii) General Behaviors of Model 1

We present in Figure 3 the SSMEM result of model 1. We show the spatial morphology reconstructed at selected frequencies (contours) in upper panels and the spectra (thin solid curves) at selected locations in lower panels.

The reconstructed maps are plotted as contours over the original model maps shown as grayscale images. The contour levels are in intervals of 10% relative to the maximum temperature of the original model. We note that the reproduced maps follow the trend of single to double sources and show relatively high dynamic range, despite the small number of visibilities. But as the source separates into a weaker one on the left and a stronger one on the right, we notice that the weaker source is so poorly reconstructed that it tends to be elongated along y axis, which is the orientation of the sparse uv distribution of the model array.

The spatially-resolved spectra shown in the lower panels are arranged to correspond to the points marked in the maps in the upper panels. The thin solid curves are the reconstructed spectra, and the thick grey curves are the model spectra. The reconstructed spectra agree well with the original model spectra, especially at regions in the vicinity of the strong source. However, the reconstructed spectrum deviates more strongly from the model spectra at the region of weaker footpoint source. At higher frequencies the intensity is underestimated. We consider this failure partly due to the increase of relative noise with frequency, which allows SSMEM more freedom to reach a higher entropy, i.e. a flatter map.

In Figure 4 we compare the images and spectra reconstructed using SSMEM (left column) with those of MEM (center column) and CLEAN (right column). In this and following figures, the maps will be shown at two frequencies 1.8 and 14.8 GHz only, and the spectra at three points, $p1$ (the stronger footpoint source), $p3$ (the weaker footpoint source) and the middle point, $p2$ (the loop-top source). At a glance the MEM result looks very similar to that of SSMEM both in map and spectrum, as somewhat expected. The MEM result shares the same systematic deviation from the true model mentioned above, i.e., the weaker left source looks flat, and the peak temperature is underestimated and decreases with frequency more rapidly than the original model. Comparing in more detail, SSMEM predicts a bit smoother spectrum and a temperature closer to the true temperature. In addition, some artificial features which are seen in MEM 14.8 GHz are suppressed under SSMEM. The suppression of such artificial features results because the position of ripples varies with frequency and maximization of spectral entropy reduces this unwanted feature.

The CLEAN images appear broader than the true sources and the images are more elongated along the y axis compared with the source because of the asymmetric CLEAN beam. As a result the intensity levels are also lower. This could be regarded as the intrinsic weakness of the CLEAN algorithm unless the beam is sufficiently round and small compared with the source. The spatially resolved spectrum would obviously depend on how good the recovery of morphology is at each frequency. After convolution with the CLEAN beams, the spectra reconstructed under CLEAN show, in overall, lower temperature than the original model, in which sense the spectra are poorly reconstructed. However we have noticed that the brightness temperature is underestimated at all frequencies more or less evenly. As a consequence, the spectral slope itself could be close to that of the original model, especially at the peak locations ($p1$, $p3$). Note however that the spectral slope at $p2$ deviates from the original model. We consider that the relatively large CLEAN beam just spreads the source temperature to the nearby locations, giving lower values at the source peaks and higher val-

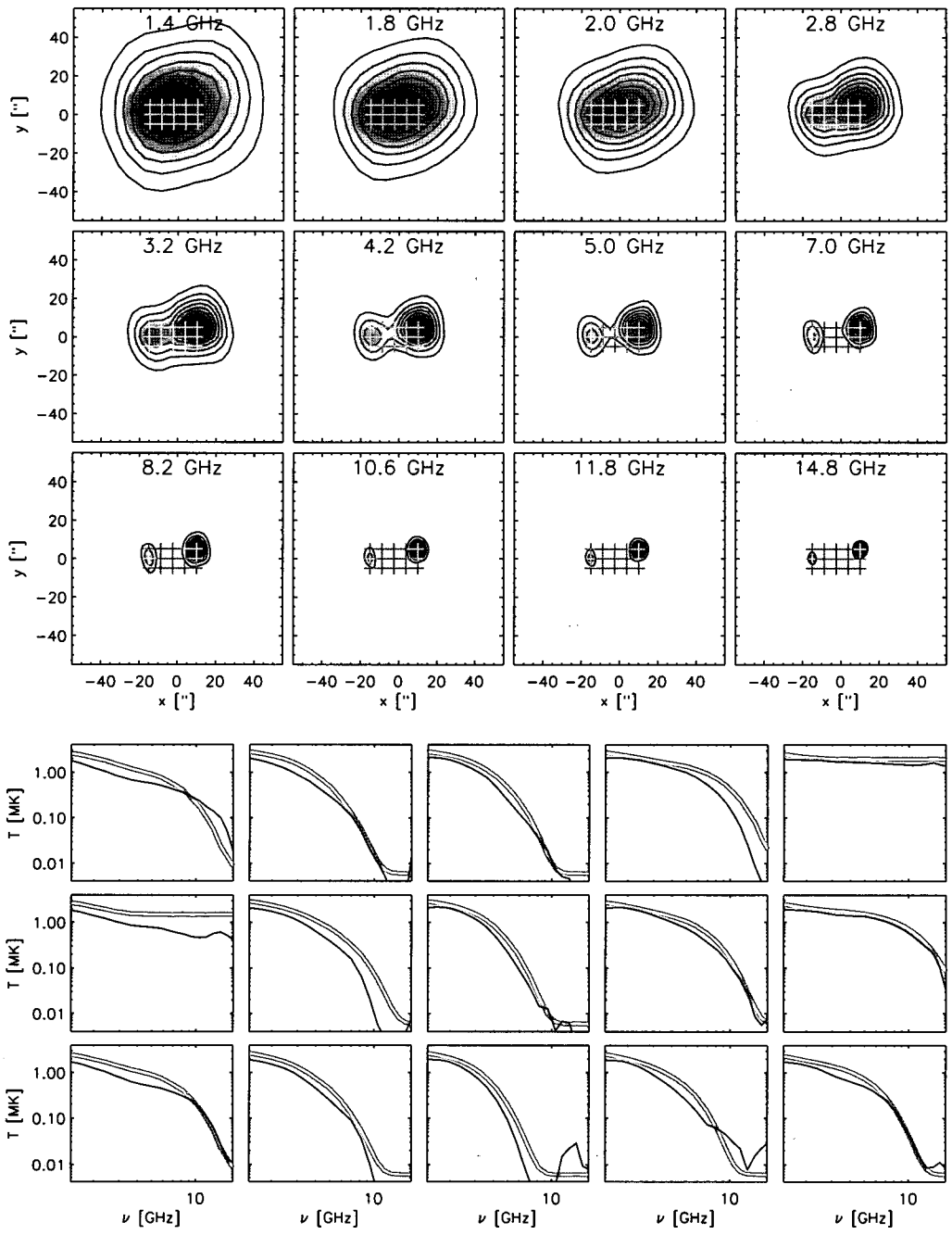

Fig. 3.— Imaging spectroscopy using the SSMEM for model 1. Upper panels show reconstructed maps and lower panels show the spatially-resolved spectra. The reconstructed maps are shown as contours and the original models as grey images at selected frequencies. Contour levels are every 10% of the original maximum temperature at each frequency. The cross symbols mark the positions selected for display of the spectrum in the lower panels. In the spectra, thin solid lines are the reconstructed spectra and thick grey lines are the original model spectra.

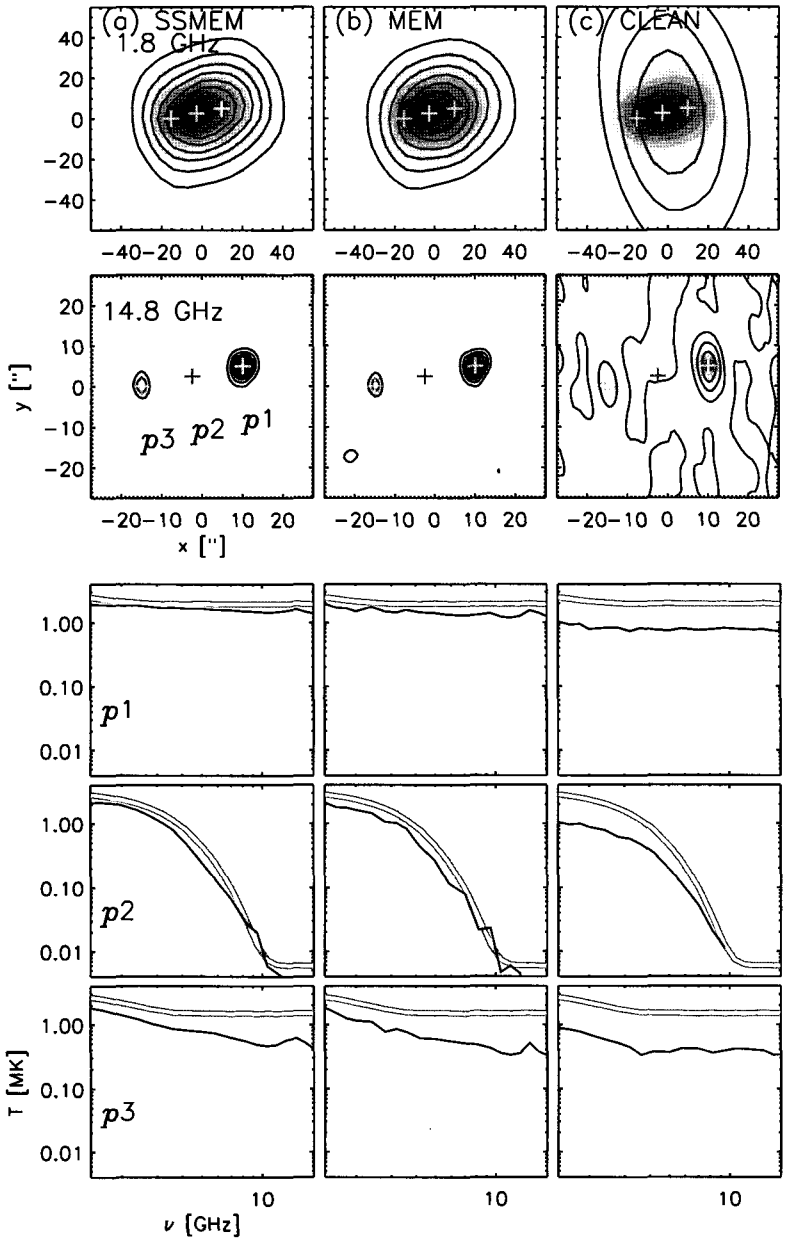

Fig. 4.— Comparison of the imaging spectroscopy made using (a) SSMEM, (b) MEM, and (c) CLEAN for model 1. For each method, maps at two frequencies, 1.8 and 14.8 GHz, and spectra at three points ($p1, p2, p3$) are shown. $p1$ and $p3$ are considered as footpoint sources, while $p2$, as a loop-top source.

ues elsewhere.

iii) Data Noise

In Figure 5 we show the result of a comparison of model 1 with models 2 and 3 in columns (a)–(c), respectively. These models differ only in the noise applied to the visibility data. As expected, in the presence of a larger amount of noise the reconstructed maps show more distorted images which are extended along the y axis compared with model 1. We can understand this as due to the fact that map values along this direction are more weakly constrained, and so the maps become flatter. Accordingly the above mentioned problem of weaker source being underestimated is more pronounced in the presence of greater noise. Regarding the reconstructed spectra, we find that model 2 (lower panels in column (b)) has led to an underestimate of the brightness temperature everywhere in the maps and model 3 (lower panels in column (c)) leads to an even greater underestimate. As the noise is dominated by the factor A in model 2, the reconstructed spectra at the peaks show relatively uniform deviation from the original model. In comparison the result of model 3 shows a greater deviation from the original at high frequency. This is because the dominance of white noise B in model 3 makes the signal to noise ratio smaller at high frequency. As a result the high frequency spectrum is underestimated while the low frequency part is well reproduced, resulting in an incorrect spectral index.

The last two columns (Figure 5(d)–(e)) show the results obtained for model 3 with MEM and CLEAN, respectively. Both show the trend of more distortion along y-axis in the presence of larger amount of noise. Just as the CLEAM map tends to be elongated along north-south because of the CLEAN beam in such shape, MEM maps also become elongated in the same direction because of the increased uncertainty in the data. The SSMEM does reduce such morphological deformation to some extent. Spectral variations are reduced under SSMEM compared with the results obtained under MEM and CLEAN. The effect of noise on both MEM- and SSMEM-derived spectra is a systematic underestimation of the temperature with increasing noise, due to the nature of the MEM algorithm (i.e., making the image flatter under increased noise). This is a tendency that must be considered in determining the spectral index through imaging spectroscopy.

In summary, we found that noise affects the map reconstruction under SSMEM or MEM in such a way that the brightness of weaker and smaller sources tends to be more seriously underestimated, and the spectral variations grow, although the stronger sources may still be well recovered. This problem of recovering weak and concentrated sources in the presence of noise is common to all methods. SSMEM produces morphology apparently similar to MEM, but performs better both in recovering spatial structure and in yielding spectral smoothness. In the example in Figure 5 the variations in the reconstructed spectrum may be considered a measure of the effect of noise, and thus smoothness in the spectrum can tell how well the reconstruction algorithm handles the noise.

iv) Source Size Variation with Frequency

We investigate how a source size variation with frequency will affect the maps and spectra obtained under SSMEM, using models 1, 4 and 5. The change of source size relative to uv coverage will be another important factor that will affect result of spectroscopic imaging. In model 1, the source changes in such a way to offset the uv change ($C = 1.0$). In Figure 6(a)–(c), we compare this with two other cases in which the source size varies with frequency faster (model 4) and more slowly (model 5) than the beam size, respectively, using power-law indexes of 1.5 and 0.5. As a consequence, model 4 has a larger source at low frequencies, in which the spatial reconstruction comes out well, but the brightness temperature is underestimated. In model 5, the source at 1.8 GHz is smaller than the beam and the reconstructed source is elongated along the y axis as due to the smaller amount of information along the v axis. Looking at the reconstructed spectra, models 4 and 5 show opposite trends: in model 4 the brightness temperatures at $p1$ and $p3$ are underestimated toward the high frequency end while in model 5 they are underestimated at low frequencies, while no characteristic frequency dependence is seen for the resulting temperature at $p2$. Therefore, for source sizes near to or smaller than the beam, a frequency-dependent source size will certainly present a problem in spectroscopic imaging.

In Figure 6(d)–(e), we compare SSMEM with other two methods using the model 5 results. MEM and SSMEM show similar results. At $p1$ both methods produce brightness temperatures that are underestimated at low and high frequencies, which is probably related to the fact that uv sampling is optimal at the middle frequencies and becomes worse at other frequencies. The deviation is substantial at the weaker footpoint source $p3$ and somehow minimal at the loop-top source $p2$. As designed, SSMEM produces a smoother spectrum than does MEM. The CLEAN spectrum approaches the model spectrum at higher frequencies at $p1$ and $p3$, as this imaging technique depends on the beam size, but CLEAN does a poor job at $p2$ at all frequencies.

The partial failure of spectral reconstruction due to an unresolved, frequency-dependent source size at some frequencies will be an unavoidable problem in any imaging spectroscopy with a fixed array. This should therefore be addressed by hardware design, e.g. scalable array (White et al. 2003). Nevertheless we can say the following. For MEM and SSMEM, the result is good at frequencies where the resolution in the uv distribution matches or exceeds the source size. Even when the

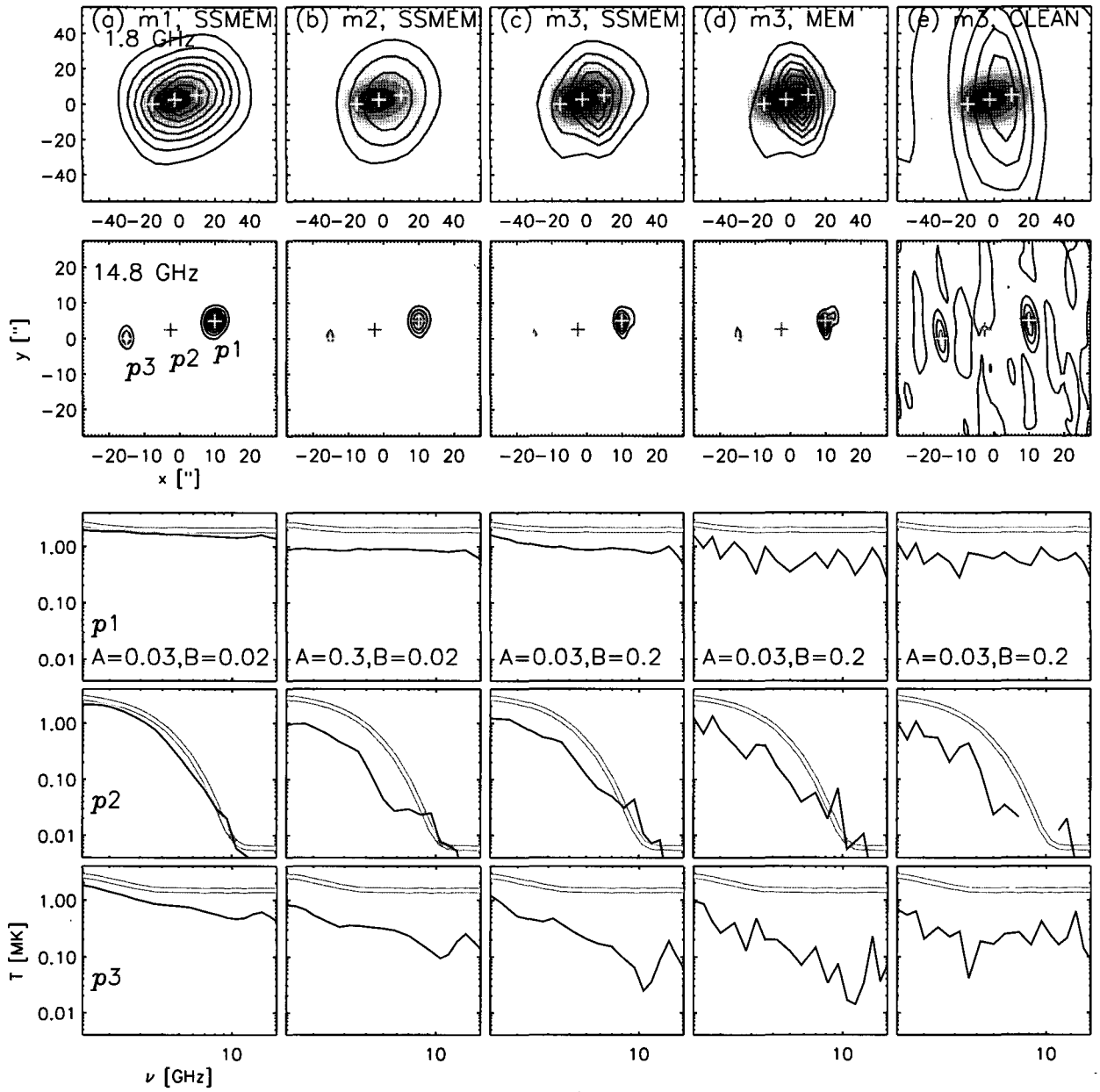

Fig. 5.— Effects of frequency-dependent noise. Results for models 1–3 are shown in the columns (a)–(c), respectively. Models 2 and 3 have enhanced noises, ($A = 0.3$, $B = 0.02$) and ($A = 0.03$, $B = 0.2$), respectively, compared with model 1 ($A = 0.03$, $B = 0.02$). Columns (d) and (e) show the results for model 3 obtained with MEM and CLEAN, respectively. Same drawing convention as in Figure 4 is used.

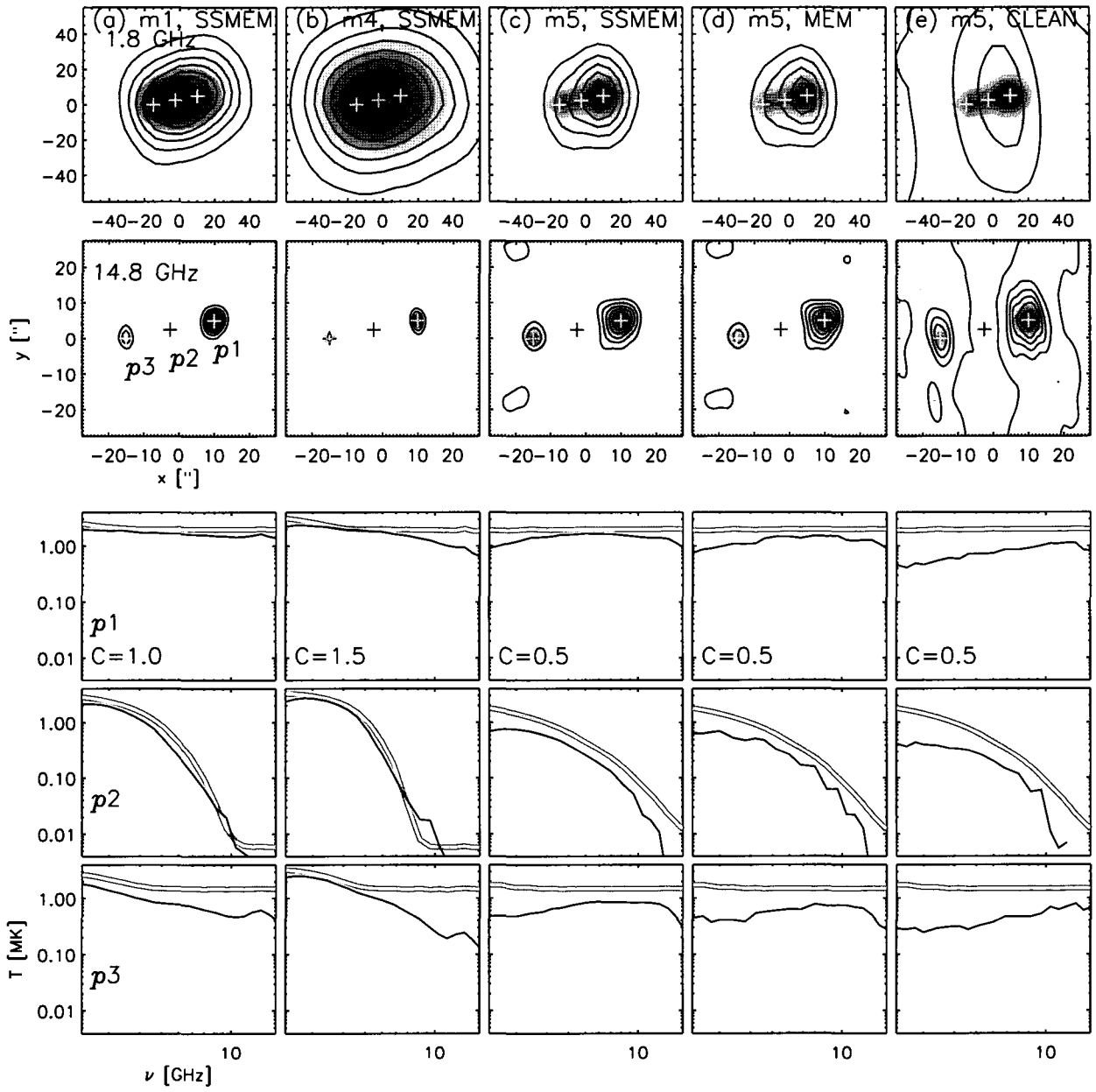

Fig. 6.— Effects of source size variation with frequency. Same drawing convention as in Figure 4 is used. The SSMEM result for model 1 is shown in column (a). The SSMEM results for models 4 and 5 are shown in (b) and (c) which have a faster ($C = 1.5$) and slower ($C = 0.5$) decrease of source diameter with frequency, respectively. Columns (d) and (e) show the result for model 5 obtained with MEM and CLEAN, respectively.

source is unresolved, the brightness temperatures are somewhat better reproduced by SSMEM than by MEM and CLEAN, due to the tendency to super-resolution offered by combining uv data at higher frequencies.

v) Contrast Between Source and Background

Finally we check how the result depends on the arbitrarily chosen background temperature. Models 6 and 7 have background temperatures set at $D = 0.03\%$ and 3% of the source maximum temperature while all the other models have 0.3%. As shown in Figure 7(a)–(c), we find that if the background is too high to make sufficient contrast against the signal (model 7), then the morphology is poorly reconstructed and the temperature is underestimated. It is therefore better to set the background flux to a low value (model 6), in which case the reconstructed image becomes sharper and the brightness temperature is fully recovered. As a cautionary remark, however, the background flux cannot be set too low, because the source temperature could be overestimated as seen in model 6 at low frequencies, where the image becomes more concentrated than the original model. In a worst case the algorithm may not proceed because of the violation of positivity (§3.1.3). It therefore appears that $D = 0.03\%$ is the optimal choice in this case. If the background flux level is properly chosen, we can minimize the above-mentioned problem that the weaker source tends to be poorly reconstructed in the presence of noise.

In Figure 7(d), we show the MEM results for model 6 (considered optimum case). The MEM and SSMEM spectra are similarly good at the strong footpoint sources $p1$. At the weaker footpoint source $p3$, the high frequency temperatures are a little more underestimated under MEM. At the loop-top source, we get larger variations in the spectrum under MEM. This shows that SSMEM can better reconstruct the spectrum than MEM, even though the morphology may look similar. In Figure 7(e), we show the CLEAN results, which are independent of the background flux. Both map and spectrum obtained with CLEAN are worse than those with SSMEM in this case.

IV. CONCLUSION

In this paper, we have outlined the basic elements of the SSMEM, and examined several issues in applying the SSMEM algorithm to solar microwave imaging spectroscopy. As a result, we have found several advantages of SSMEM in comparison with MEM and CLEAN algorithm. (1) As we use a highly eccentric array configuration, a major drawback with CLEAN appears that the map resembles the beam shape in snapshot mode. At modest amount of noise the SSMEM overcomes the uneven uv distribution by searching a global solution in frequency and space. (2) The SSMEM can to some extent suppress noise to produce a smoother spectrum than other techniques. In some cases it can help in the removal of sidelobes better than MEM and CLEAN. (3) SSMEM in the present form is particularly good for reproducing the large, optically thick source. Both morphology and temperature are closely reproduced under SSMEM whereas CLEAN tends to produce a distorted source shape, systematically underestimates the temperature, and produces spectra with large variations. At present SSMEM results are presented without convolution with the CLEAN beam. (4) SSMEM more or less faithfully maintains the diversity of spectra depending on the spatial positions, whereas CLEAN seems to make spectra distorted by that of the maximum brightness region. Maybe it tends to transfer the peak region spectrum to nearby regions. We thus conclude that the present SSMEM performs better imaging spectroscopy than MEM and CLEAN.

The results presented in this paper may be used as a guide in applying SSMEM to sun-like radio sources which have frequency-dependent size and intensity. We have shown that the intrinsic source variation in the presence of frequency-dependent noise will make the imaging spectroscopy a challenging task. While we have shown SSMEM can address the problem to produce a smoother spectrum than the other imaging techniques, this does not mean that SSMEM is immune to all difficulties arising due to intrinsic source variation with frequency. For instance, we have shown that a weaker and smaller source in the presence of relatively high noise tends to be spread out due to entropy being less constrained by the data, and thus the brightness temperature is underestimated. Worse, under solar conditions this may distort the spectra due to a progressive drop in brightness temperature with frequency due to the source (usually one of asymmetric footpoint sources) becoming weaker with increasing frequency. In this case SSMEM can lead to a systematic bias in the spectral index determination, while elsewhere providing a correct spectral index for brighter sources. At present, it appears that adjusting the background flux arbitrarily with frequency is a simple remedy in optimizing the fidelity in spectral reconstruction. In spite of such unavoidable problems, which are common to any imaging algorithm, our results show that SSMEM is preferred for imaging spectroscopy in that it provides a global solution in the maps and spectra under consistent treatment at all frequencies, and further its rationale matches the scientific goals that we have for imaging spectroscopy.

The issues discussed in this paper are most relevant to solar imaging spectroscopy, while they can also apply to other types of Fourier-Transform imaging of astronomical objects at multifrequencies. At radio wavelengths, the SSMEM can be used with the currently available solar array, OVSA, and in future, the Frequency-Agile Solar Radiotelescope (FASR). The Enhanced Very Large Array (EVLA) data will also be amenable to use of SSMEM. Fourier-transform imaging is also employed in solar hard X-ray observations with, for instance, the Hard X-ray telescope (HXT) on-

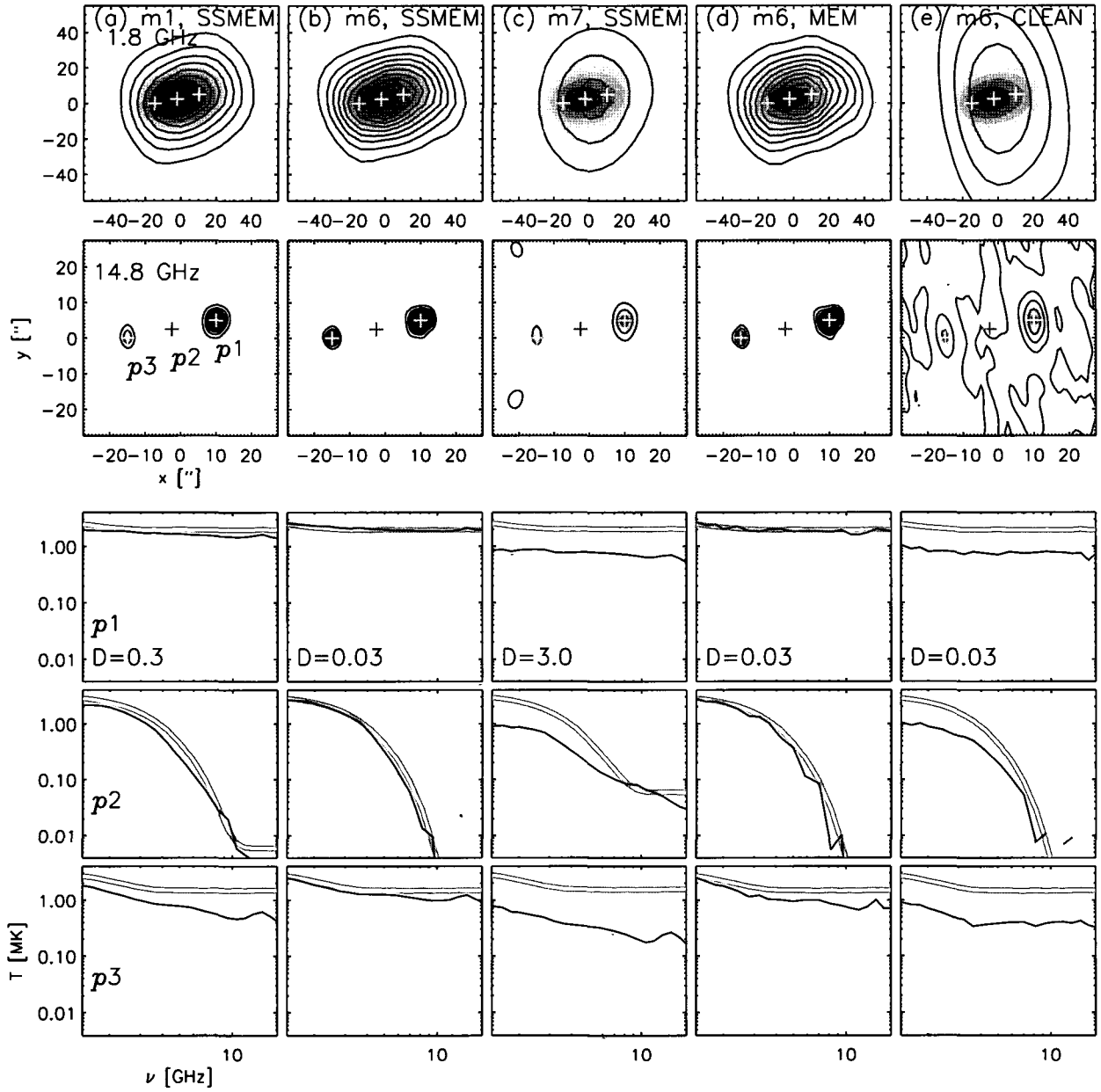

Fig. 7.— Effects of background flux variation with frequency. Models 6 and 7 have a lower (D = 0.03%) and higher (D = 3.0%) contrast of peak-to-background temperature compared with D = 0.3% used for all other models. The results are shown in (b) and (c), respectively, along with model 1 in column (a). Columns (d) and (e) show the results for model 6 obtained with MEM and CLEAN, respectively.

board Yohkoh, and the Reuven Ramaty High Energy Solar Spectroscopic Imager (RHESSI). In radio imaging, we find that the NR method could be preferred for computational efficiency. In the hard X-ray imaging with RHESSI, however, we were informed that the synthesized beam varies depending on the position within maps, which makes the diagonalization approximation invalid. In the latter case, we recommend to use the CG method instead. Currently we are collaborating with a NASA team (Dr. E. J. Schmahl, private communication) to develop another version of SSMEM for use with the hard X-ray data obtained with the RHESSI.

ACKNOWLEDGEMENTS

One of us (SB) was financially supported by the BK21 Project of Ministry of Education, the KOSEF grant R14-2002-043-0100-0, and the MOST Fund of M1-0407-00-0001 in Korea. JL has been supported by NSF grants AST-0138317 and NASA Grant NAG 5-10891. The OVSA is supported by NSF grant AST-0307670 and NASA grant NAG5-11875 to New Jersey Institute of Technology.

APPENDIX A. NOISE AND SIGNAL IN SOLAR VISIBILITY

We consider the correlated signal from two antennas. One antenna has signal p and noise P and the another antenna has q and Q. Then the correlated signal is $V = (P+p)(Q+q)$ and the true visibility is $\langle V \rangle = pq$. Here, $\langle\rangle$ represents the expectation value.

For astronomical objects, the noise typically dominates the signal ($|P| \gg |p|$) and any terms containing the noise (Pq, Qp, and PQ) can be averaged out after long time integration. For the sun, the opposite is true and the correlation terms can survive. Under this idea, we consider the range of possible form of the variance in visibility amplitude. If $|p| \approx |q|$ and $|P| \approx |Q|$ and further $|p| \gg |P|$, the variance in V can be approximated to

$$\sigma^2 = \langle |V - \langle V \rangle|^2 \rangle \approx \langle |pQ + qP|^2 \rangle \propto |pP|^2 \qquad \text{(A1)}$$

On general grounds, we can consider three cases. First, the noise $|P|$ is just independent of the signal, $|p|$, in which case we will have the standard deviation σ depending on the visibility amplitude $|V|$ as

$$\sigma \propto |p| \propto |V|^{1/2} \qquad \text{(A2)}$$

Second, as more likely, the noise $|P|$ may be proportional to the square root of the signal, $|p|$, in which case we have

$$\sigma \propto |p|^{3/2} \propto |V|^{3/4} \qquad \text{(A3)}$$

Finally, we consider a somewhat extreme case where the $|P| \propto |p|$. In this case we will have

$$\sigma \propto |p|^2 \propto |V| \qquad \text{(A4)}$$

In the paper we take the latter form which gives the strongest dependence of noise on the signal in the measured visibility.

REFERENCES

Aschwanden, M. J., Schmahl, E. J., & The RHESSI team, 2002, Reconstruction of RHESSI Solar Flare Images with a Forward Fitting Method, Sol. Phys., 210, 193

Bong, S.-C., Lee, J., Gary, D. E., & Yun, H. S., 2005, Spatio-Spectral Maximum Entropy Method: I. Formulation and Test, ApJ, in press (Paper I)

Conway, J. E., Cornwell, T. J., & Wilkinson, P. N., 1990, Multi-Frequency Synthesis: a New Technique in Radio Interferometric Imaging, MNRAS, 246, 490

Cornwell, T. J., Braun, R., & Briggs, D. S., 1999, Deconvolution, in ASP Conf. Ser. 180, Synthesis Imaging in Radio Astronomy II, ed. G. B. Taylor, C. L. Carilli, & R. A., Perley (San Francisco: ASP), 151

Cornwell, T. J. & Evans, K. F., 1985, A Simple Maximum Entropy Deconvolution Algorithm, A&A, 143, 77

Dulk G. A., 1985, Radio Emission from the Sun and Stars, ARA&A, 23, 169

Gary, D. E. & Hurford, G. J., 1994, Coronal Temperature, Density, and Magnetic Field Maps of a Solar Active Region Using the Owens Valley Solar Array, ApJ, 420, 903

Gary, D. E. & Hurford, G. J., 1999, OVRO Solar Array Upgrades in Preparation for MAX 2000, in NRO Rep. 479, Solar Physics with Radio Observation, Proceedings of the Nobeyama Symposium, held in Kiyosato, Japan, Oct. 27-30, 1998, ed. T. S. Bastian, N. Gopalswamy & K. Shibasaki (NRO), 429

Gull, S. F. & Daniell, G. J., 1978, Image Reconstruction from Incomplete and Noisy Data, Nature, 272, 686

Högbom, J. A., 1974, Aperture Synthesis with a Non-Regular Distribution of Interferometer Baselines, A&AS, 15, 417

Komm, R. W., Hurford, G. J., & Gary, D. E., 1997, A Spatial and Spectral Maximum Entropy Method as Applied to OVRO Solar Data, A&AS, 122, 181

Melrose, D. B., 1980, Plasma Astrophysics, Vol. 1 (New York: Gordon and Breach Sci. Publ.)

Narayan, R. & Nityananda, R., 1986, Maximum entropy image restoration in astronomy, ARA&A, 24, 127

Press, W. H., Teukolsky, S. A., Vetterling, W. T., & Flannery, B. P., 1992, Numerical recipes in C: The Art of Scientific Computing (2nd ed.; Cambridge: Cambridge Univ. Press)

Sault, R. J., 1990, A Modification of the Cornwell and Evans Maximum Entropy Algorithm, ApJ, 354, L61

Sault, R. J. & Wieringa, M. H., 1994, Multi-Frequency Synthesis Techniques in Radio Interferometric Imaging, A&AS, 108, 585

Schmahl, E. J. & Hurford, G. J., 2002, RHESSI Observations of the Size Scales of Solar Hard X-Ray Sources, Sol. Phys., 210, 273

Skilling, J. & Bryan, R. K., 1984, Maximum Entropy Image Reconstruction: General Algorithm, MNRAS, 211, 111

Wernecke, S. J. & D'Addario, L. R., 1977, Maximum Entropy Image Reconstruction, IEEE Trans. Comput., C-26, 351

White, S. M., Lee, J., Aschwanden, M. J., & Bastian, T. S., 2003, Imaging Capabilities of the Frequency Agile Solar Radiotelescope (FASR), in Proc. of the SPIE, 4853, Innovative Telescopes and Instrumentation for Solar Astrophysics, ed. S. L. Keil, & S. V. Avakyan (SPIE), 531